CHEMISTRY OF MATERIALS

pubs.acs.org/cm

Article

Effect of Annealing on the Structure, Composition, and Electrochemistry of NMC811 Coated with Al_2O_3 Using an Alkoxide Precursor

Víctor Riesgo-González, David S. Hall, Katharina Märker, Jonathan Slaughter, Dominic S. Wright, and Clare P. Grey*

Cite This: Chem. Mater. 2022, 34, 9722−9735

Read Online

ACCESS | Metrics & More | Article Recommendations | Supporting Information

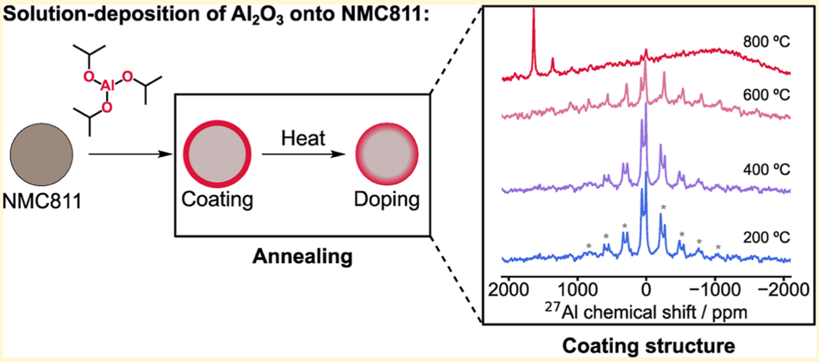

ABSTRACT: Nickel-rich layered oxides are promising positive electrode materials for lithium-ion batteries due to their high capacity and decreased cobalt content. The application of surface coatings is a common approach to slowing or potentially stopping deleterious reactions at the electrode−electrolyte interface of lower-Ni content layered oxides. However, their efficacy on Ni-rich $LiNi_{0.8}Mn_{0.1}Co_{0.1}O_2$ (NMC811) is less certain, and knowledge on how to design effective coatings with favorable properties is sparse. In this work, we develop a convenient solution-based deposition method for the synthesis of aluminum oxide coated NMC811 secondary particles and we study the effects of annealing temperature on their structure and electrochemical lifetime in lithium-ion batteries. Using energy-dispersive X-ray spectroscopy and X-ray fluorescence spectroscopy, we quantify the amount and distribution of aluminum oxide on the cathode particles. Changes in the coating phase and composition as a function of annealing temperature are tracked with solid-state nuclear magnetic resonance and X-ray photoelectron spectroscopy. ^{27}Al NMR spectroscopy at very high fields (23.5 T) provides direct evidence that after annealing up to 400 °C, 4-, 5-, and 6-coordinate aluminum is present, here assigned to an amorphous alumina coating, but after annealing to 600 °C, a γ-$LiAlO_2$-like coating is observed. We further differentiate between Al in the bulk and surface phase and identify, for the first time, the critical temperature at which doping occurs in NMC811. Surface/bulk doping starts to occur in the range of 500−600 °C, with considerable bulk doping being found at 800 °C. The onset of Al diffusion coincides with the decrease in capacity retention, contradicting previous studies and giving new insight into the relationship between lifetime and lithium-ion conductivity.

INTRODUCTION

Developing cathodes with higher capacities and lower costs is a key challenge in lithium-ion battery research. The strategy most widely used in batteries designed for the electric vehicle (EV) market is to replace Co by Ni in the parent cathode material, $LiCoO_2$ (LCO). $LiNiO_2$ (LNO) achieves higher capacities at similar voltages as compared to LCO, and Ni is also cheaper and associated with fewer environmental/mining concerns than Co. On the other hand, the stability of LNO is worse than that of LCO, particularly as more Li is removed during battery operation. This has led to the development of a wide range of $Li[Ni_xMn_yCo_z]O_2$ (NMC) compounds to improve upon the stability of LNO whilst maintaining high capacities.[1,2] For example, by synthesizing and testing NMC materials with varying amounts of nickel, Noh *et al.* found that higher nickel content led to higher capacity but at the cost of faster capacity fade and safety issues.[3] Subsequent studies of Ni-rich materials such as NMC811 (where $x = 0.8$ and $y = z = 0.1$) have shown that degradation becomes particularly

Received: August 22, 2022
Revised: September 22, 2022
Published: October 17, 2022

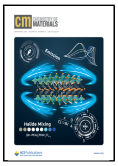

https://doi.org/10.1021/acs.chemmater.2c02580

pronounced when cycling to upper cutoff voltages where more than 80% of Li is removed (above 4.2 V for NMC811 *vs* graphite).[4,5] Accordingly, excellent lifetimes are achievable in NMC811/graphite cells operated under more moderate conditions (*e.g.*, 3.00−4.06 V and 20−30 °C).[6] Improvements in battery lifetime can also be attained by modifying the NMCs through surface coatings[7−15] or by using electrolyte additives.[16−18] Even with these strategies, it is not yet clear whether it is possible to obtain satisfactory performance at temperatures above 25 °C or with increased voltage windows for practical applications.

One proposed major mechanism for degradation of NMC materials is related to the exergonic loss of lattice oxygen at delithiated states of charge and the formation of densified phases such as spinel (M_3O_4, with M = Ni, Mn, and Co) and rock salt (MO) on the surface of the cathode particles upon exposure to the electrolyte.[19,20] These insulating and electrochemically inactive layers grow with cycling, particularly at high voltages, leading to a decrease in capacity.[21] One potential strategy to mitigate this is to modify the positive electrode by coating its active surface with a protective layer to limit exposure to the electrolyte. A plethora of coating materials have now been investigated. Some of the most common materials used to coat NMC cathode particles include metal oxides such as Al_2O_3,[7−9] TiO_2,[22] ZrO_2,[15] and SiO_2[10] but also metal phosphates and fluorides like $AlPO_4$,[23] $FePO_4$,[11] AlF_3,[12] CaF_2,[24] and $LiAlF_4$.[13] These coatings can be deposited using vapor-deposition techniques such as atomic layer deposition (ALD)[14,25,26] or solution-based methods which do not require sophisticated equipment and tend to be easier to scale up.[7−9,27,28]

Al_2O_3 has a number of desirable properties compared to other oxides that make it stand out as a coating material. Aluminum is non-toxic and the most abundant metallic element in the Earth's crust. Al_2O_3 coatings lead to the *in situ* formation of $LiPO_2F_2$, a well-known electrolyte additive, by reaction with $LiPF_6$, and in contrast with other oxide coatings such as Nb_2O_5 and TiO_2, it has been shown to inhibit the reactions involving ethylene carbonate (EC), which limits a cascade of degradation mechanisms.[25,29]

Despite Al_2O_3 being one of the most extensively studied cathode coating materials, there is still a need for practical methods to synthesize Al_2O_3-coated nickel-rich particles. There is also a limited understanding of the effects of synthetic conditions, such as annealing temperature, on the structural and electrochemical properties of the material. The coatings are proposed to protect the outer surface from contact with the electrolyte,[30] and surface doping may suppress the near-surface rearrangements that lead to rock-salt formation and growth without sacrificing specific capacity as bulk doping with aluminum increases the thermal stability and capacity retention of lower nickel-content NMCs by delaying oxygen loss and retarding transformation to spinel.[31−34] However, these hypotheses still need further experimental verification. While some previous studies have found that the Al_2O_3 coatings improved capacity retention in NMCs with a 70% nickel content or lower, there is more divergence of opinions about the effect that Al_2O_3 coatings have on the degradation of NMC cathodes with 80% nickel or higher. For example, Han *et al.* found that Al_2O_3 coatings had a negative effect in overall capacities and capacity retention in NMC811 cathodes and that annealing further deteriorated performance, which they ascribed to the diffusion of aluminum cations from the coating into the bulk of the material.[35] Others, like Neudeck *et al.*, observed an increase in capacity retention after coating NMC811 with Al_2O_3 from solution using trimethyl aluminum (TMA) as a precursor.[8]

Several coating methods have been developed to deposit Al_2O_3 coatings onto cathode materials. ALD is one of the most common methods to coat NMC and LCO with a layer of Al_2O_3 and generally leads to improvement in capacity retention and stability.[14,29,36,37] Another possibility is to use solution-based coating methods (wet chemistry), with early work in this area showing that the deposition of Al_2O_3 coatings onto LCO has a positive effect on capacity retention. Cho *et al.*[38,39] coated LCO with Al_2O_3 using an alkoxide precursor (aluminum ethylhexanodiisopropoxide) solution in isopropanol following a sol−gel route. The coating process was explained in terms of hydrolysis of the precursor by either ambient moisture or −OH groups present on the surface of LCO. They found that annealing of the coated LCO led to the diffusion of the coating into the particles as well as surface doping. Others used aluminum and lithium salts to coat LCO. For example, Chen *et al.* used an $Al(NO_3)_3 \cdot 9H_2O$ and $LiNO_3$ solution in ethanol to coat nano-LCO with $LiAlO_2/Al_2O_3$.[40] Similarly, Han *et al.* used an aqueous $Al(NO_3)_3$ solution to coat both LCO and NMC523 and studied the evolution of the coating layer as a function of annealing temperature.[41] Dogan and co-workers have, in extensive and careful studies, built on this work and examined a variety of different nitrate and alkoxide precursors dissolved in different solvents and have compared the resulting coatings with those deposited with ALD.[27,35,41,42] Other recent studies have used TMA in organic solvents as the precursor solution.[7,8,28] TMA forms aluminum oxide by reaction with water through cleavage of the Al−C bonds (hydrolysis) generating methane.

In this work, we develop a scalable and cheap method for coating cathode particles with Al_2O_3 using a solution deposition route and a molecular precursor, aluminum isopropoxide. This precursor is deposited over the surface of the NMC811 particles and is decomposed by annealing, leading to a layer of oxide coating. Our coating method differs from previously reported ones: as discussed above, many previous studies have used conventional sol−gel approaches in which aqueous solutions with aluminum nitrate or aluminum alkoxides in organic solvents are used to coat cathode particles with Al_2O_3 by slow evaporation of the solvent.[9,27,43,44] However, because NMC811 is carbon dioxide- and moisture-sensitive, this can potentially lead to degradation during the deposition process if it is not done under inert conditions.[45] In contrast, our method allows the deposition directly from solution by using molecular precursors that react with the surface of the NMC under nitrogen and that can be decomposed later by annealing, leading to the metal oxide coating.[46] This allows us to avoid water and carbon dioxide completely and should produce thinner and more homogeneous coatings since, unlike in other synthesis routes, we remove the solution containing the unreacted precursors. Here, we use aluminum isopropoxide (AIP) in toluene as the precursor solution. AIP is an aluminum alkoxide which forms aluminum oxide by hydrolysis (*e.g.*, by reaction with surface OH groups) or thermolysis but is not pyrophoric, making it safer than TMA and more suitable for large-scale production. Compared to the aluminum ethylhexanodiisopropoxide used by Cho *et al.*,[38] AIP should hydrolyze more readily as alkoxide ligands are more basic than carboxylates. Furthermore, our coating process is followed by annealing of the coated particles.

We present a detailed characterization of the Al_2O_3 coatings deposited on NMC811 using the synthesis method described above, focusing especially on the effects of different annealing temperatures. Scanning electron microscopy (SEM), transmission electron microscopy (TEM), energy-dispersive X-ray spectroscopy (EDS), X-ray photoelectron spectroscopy (XPS), and ^{27}Al nuclear magnetic resonance (NMR) spectroscopy are applied to uncover the structural, morphological, and compositional changes of the coatings that take place at different annealing temperatures. Finally, we relate these changes to the electrochemical performance of the coated cathode materials by performing long-term galvanostatic cycling of half cells and compare our results to previous coating studies.

■ EXPERIMENTAL SECTION

Synthesis of Al_2O_3-Coated NMC811. This procedure was carried out under an inert, dry nitrogen atmosphere. 10 g of NMC811 (Targray) and 100 mg of aluminum isopropoxide (AIP, Sigma-Aldrich) were loaded into two separate Schlenk tubes inside a glovebox. The two flasks were connected to a nitrogen line, and 50 mL of dry toluene was added to each flask. The precursor solution was then added to the NMC811 suspension, and the mixture was left to react for 48 h at 80 °C stirring. The mixture was allowed to cool to room temperature, and the solvent was removed using a syringe. The solid was washed three times with dry toluene in order to remove any unreacted precursor by adding 10 mL of toluene, stirring, and removing it with a syringe. The product was then dried at 100 °C under vacuum (10^{-2} atm, 1 h). For samples annealed at higher temperatures, the annealing was performed for 4 h under air at temperatures between 200 and 800 °C. As a control, one sample was also annealed at 800 °C under oxygen. Further control samples were synthesized following the same procedure described above, but without the addition of AIP.

Electrode Fabrication. Electrodes were prepared by mixing 88 wt % NMC811 powder with 6 wt % carbon black (Super-P Carbon, Timcal) and 6 wt % PVDF binder (Kynar, HSV-900). The total amounts of the coated and uncoated solids ranged between 250 and 400 mg. The solid mixture was ground for 5 min under air using a pestle and mortar. Then 0.85 mL of *N*-methyl-2-pyrrolidone (NMP) per gram of solid was added; the slurry was mixed in a planetary centrifugal mixer (Thinky, ARM/310 CE) at 2000 rpm for 10 min and transferred to a nitrogen-filled glovebox. Here, the slurry was cast on aluminum foil with a doctor-blade to 150 μm thickness. The cast electrode was then dried under vacuum at room temperature overnight and cut into electrode disks of 12.7 mm diameter. These were dried under vacuum at 120 °C for 24 h before being transferred to an argon-filled glovebox with oxygen and water levels below 10 ppm. The resulting electrodes had active mass loadings of 6.4 ± 1.4 mg/cm^2.

Cell Assembly and Galvanostatic Cycling. Coin cells were assembled inside an argon-filled glovebox with water and oxygen levels below 10 ppm. The cell components were a lithium disk of 16 mm diameter, purchased from LTS Research Laboratories, Inc. as the counter electrode, one 0.5 mm thick spacer, a steel spring, a glass fiber separator (GF/B, Whatman, 16 mm diameter) soaked with 100 μL of electrolyte, and the cathode disk. The electrolyte used was 1.0 M $LiPF_6$ in ethylene carbonate (EC) and ethyl methyl carbonate mixed in a 3:7 w/w ratio (SoulBrain, USA). The cells were cycled between 3.0 and 4.3 V. After two formation cycles at C/20, the cells were cycled at C/2 for 250 or 300 cycles, with two diagnostic cycles at C/20 every 50 cycles. In this work, 1 C refers to the current needed to charge or discharge the cell in 1 h with an upper cutoff voltage of 4.3 V (corresponds to a cathode capacity of ∼200 mA h/g). After electrochemical testing, the cells were stored in the discharged state for post-mortem analysis for 15 months.

X-ray Fluorescence Measurements. Measurements were performed using an Epsilon 4 Malvern Panalytical X-ray fluorescence (XRF) spectrometer with a Ag anode (an X-ray energy of 50 kV) and a SDD30 silicon drift detector.

Solid-State NMR Experiments. Measurements were carried out on a 16.4 T Bruker Avance III spectrometer (700 MHz ^{1}H Larmor frequency) using a Bruker 1.3 mm magic-angle spinning (MAS) probe. All samples were as-coated powders, except for the one annealed at 800 °C under air which was scraped from an electrode. Sample quantities ranged between 7.6 and 9.3 mg. Experiments were performed at 50 kHz MAS frequency using a Hahn-echo pulse sequence with a 100 ms recycle delay and a total echo length of two rotor periods (40 μs). Between 372,000 and 402,000 scans (free induction decays) were acquired, leading to experimental times between 14 and 17 h. AlF_3 (−17.0 ppm) was used as an external reference to calibrate the ^{27}Al chemical shift.

The high-field NMR measurements were performed on a 23.5 T Bruker Avance Neo spectrometer (1 GHz ^{1}H Larmor frequency) with a Bruker 1.9 mm MAS probe. All samples were as-coated powders. Experiments were performed at 40 kHz MAS frequency for the samples annealed at 200 and 600 °C and at 38 kHz MAS frequency for the sample annealed at 400 °C. Again, a Hahn-echo sequence was used with a recycle delay of 100 ms and a total echo length of two rotor periods. Between 684,416 and 715,520 free induction decays were collected, leading to experimental times between 21 and 23 h. The spectra were simulated and fitted using a Czjzek distribution[47] (Gaussian isotropic model, $d = 5$) as implemented in the DMFit software ("CzSimple" model).[48]

Scanning Electron Microscopy. Images were taken with a TESCAN MIRA3 Field emission gun (FEG) (for SEM) in the secondary electron (SE) mode with beam voltages ranging from 2 kV for the pristine NMC and 5 kV for the coated samples. The working distance was 6 mm for all images. All samples were coated with 10 nm of Cr before imaging using a Quorum Technologies Q150T ES Turbo-Pumped Sputter Coater/Carbon Coater. For the elemental quantification using energy-dispersive X-ray spectroscopy (EDS), between 20 and 100 point scans were taken on different regions of each sample. All EDS measurements were performed using a 15 keV electron beam and with a working distance of 15 mm. To prepare the cycled samples for SEM, the coin cells were opened inside an argon glovebox, and the electrodes were washed with dimethyl carbonate three times to remove the electrolyte and dried under vacuum, and the electrode material was scraped off the current collector.

Transmission Electron Microscopy. The samples for TEM imaging were prepared by drop-casting a suspension of the NMC811 particles in ethanol onto a lacey carbon-coated copper grid (EM Resolutions, 300 mesh), followed by solvent evaporation. For the cycled samples, this was preceded by opening the coin cells inside an argon glovebox, washing the electrodes with dimethyl carbonate three times to remove the electrolyte, drying under vacuum, and scraping the electrode material off the current collector. TEM images, scanning TEM (STEM), and EDS spectra and maps were collected using a Thermo Scientific (FEI) Talos F200X G2 TEM operating at 200 kV with a spot size of 5 and 70 μm aperture for the bright-field (BF) imaging. TEM images were acquired using a Ceta 16M CMOS camera. EDS was performed in the STEM mode with images acquired using the high-angle annular dark field (HAADF) and bright field (BF) detectors and EDS spectra/maps collected using the Super-X EDS detector system which consists of four windowless silicon drift detectors. Between 1 and 3 maps were collected in different regions of the sample for the as-coated and cycled samples. Surface and bulk Al:Ni ratios were extracted from relevant areas of those maps. The thickness of the coatings was estimated by measuring the coating thicknesses from TEM images taken on different regions of the sample and using both HR-TEM and STEM images (Figures S37−S40 and Table S7 for the thickness measurements).

X-ray Photoelectron Spectroscopy. The XPS spectra were measured using an Escalab 250Xi spectrometer. An aluminum Kα X-ray source was used. The spot size was 500 μm for all measurements. For the high-resolution spectra, 20 eV of pass energy and 0.1 eV step size were used. A total of 60 and 20 scans were measured for the Al 2p and the C 1s spectra, respectively.

Powder X-ray Diffraction. The powder X-ray diffraction (PXRD) data were collected on a Panalytical Empyrean powder X-ray diffractometer using Cu Kα radiation (λ = 1.541 Å) over the 2θ range of 5−80° for 1 h. Rietveld refinements were performed to obtain lattice parameters and site occupancies using the TOPAS program (V6).[49]

RESULTS

Coating Synthesis. To study the effect of Al_2O_3 coatings on the degradation of NMC811, we started by developing a solution-based method for the deposition of Al_2O_3 onto the surface of NMC secondary particles, which were roughly spherical aggregates of the NMC811 primary particles. The NMC811 particles were suspended in a solution of AIP (1% of the total solid weight) in toluene and mixed for 2 days at 80 °C before removing the excess solvent. After washing the sample with toluene to remove the excess AIP, the product was dried at 100 °C for 1 h under vacuum. Next, the particles were annealed under air for 4 h (Figure 1). Since AIP is known to react with water, the aim here was to exploit the trace amounts of water or hydroxyl groups, present on the NMC811 particles, to deposit an aluminum-based layer. Several weight % of AIP (1, 2, and 40%, the latter primarily for NMR studies) were tested initially, but it was found that the electrochemical performances of the 2 wt % and especially the 40 wt % precursor samples were poor, so only the results for the 1 wt % samples are reported here. Several temperatures were used for the annealing step (200, 300, 400, 500, 600, 700, and 800 °C); this step is introduced to ensure the full decomposition of the precursor, to induce changes in the structure of the coating, and to explore the diffusion of the aluminum ions into the sub-surface of the particles to achieve surface doping. Uncoated samples annealed at 400 and 800 °C under air were also prepared to investigate the effect of annealing under air on the structure and electrochemical cycling of NMC811, allowing us to separate this contribution from the effect the coating on the degradation of the material. These samples were treated with toluene at 80 °C for 48 h under nitrogen but without adding AIP and then annealed at either 400 or 800 °C under air for 4 h. Finally, since NMC811 is synthesized under an oxygen atmosphere,[2] a coated sample annealed at 800 °C under oxygen was synthesized to test whether annealing under air at high temperatures may be degrading the material, leading to faster capacity fade, and if the capacity retention of coated NMC811 can be improved further by annealing under oxygen.

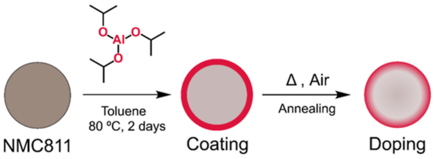

Figure 1. Coating process consists of two steps; the deposition of the precursors onto the surface of the NMC811 secondary particles from solution and the annealing of the resulting product.

Surface Characterization. In order to verify the presence of a coating and to determine its thickness, morphology, and composition, a variety of surface-sensitive techniques were used. First, the coating morphology and the changes it undergoes at increasing annealing temperatures were determined by SEM. Representative SEM images of the pristine and coated secondary particles discussed in this work are shown in Figure 2, with further images shown in the Supporting Information (Figures S1−S19). From the SEM images, we can see that the NMC811 primary particles are 100−200 nm in diameter and that they are agglomerated into spherical secondary particles of 5−20 μm in diameter. After coating and annealing up to 500 °C, the primary particles are covered by a thin layer of material, with the surface becoming smoother and the primary particles being no longer as clearly visible. Small coating particles of 0.5−1 μm are also observed on top of the thin layer. At higher annealing temperatures, there is a further change in the surface morphology of the particles. The surface becomes rougher, and the primary particles are more clearly resolved. SEM images of the samples annealed at 200 and 400 °C after 250 and 300 electrochemical cycles show full secondary particles that retained the smooth morphology observed for the non-cycled samples (Figures S20 and S21).

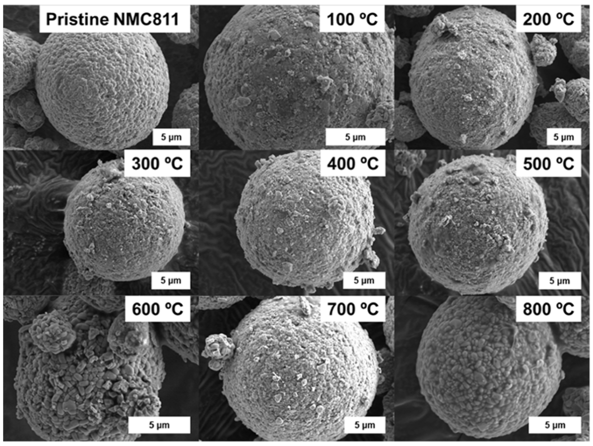

Figure 2. SEM images of uncoated (pristine) NMC811 particles and of NMC811 particles coated with Al_2O_3 and annealed at different temperatures, as given in the figure. The sample labeled as “100 °C” was only dried for 1 h under vacuum and not annealed under air. Images of samples annealed at 200−500 °C show a layer of material that has been deposited, changing its surface morphology with annealing temperature. After annealing at temperatures of 600−800 °C, the primary particles become again more visible. This is attributed to a densification of the coating layer and its diffusion into the bulk of the material.

Next, TEM imaging was performed on the samples annealed at 200, 400, 600, and 800 °C to investigate the morphology of the coating layer further and to determine the thickness of the coating (Figures S22−S26 and S37−S40 and Table S7). TEM shows the presence of a layer of material on top of the coated particles regardless of the annealing temperature but not in the pristine samples. The thickness of the coating was estimated by measuring the length of the coating at selected areas in different TEM and STEM images for each sample. It was found that the thickness varies greatly depending on the region of the sample under examination, but overall, fewer thick coating regions were found in the high-temperature annealing samples (Table S7).

To prove that the deposited films are aluminum-based and to study if there is diffusion of the coating into the bulk of the particles, we next determined the surface composition of the coated and annealed samples using a combination of surface-sensitive techniques, XRF, SEM-EDS point scans, STEM-EDS maps, and XPS measurements.

Both SEM-EDS and XRF results confirm the presence of aluminum on the surface of the coated NMC811 and that the pristine NMC811 does not contain aluminum (Figures S10 and S11 and Tables S1, S8 and S9). This was further verified by STEM-EDS, which shows that the coating layer contains aluminum (Figures 3a, S29−S36 and Tables S3−S6). To compare the aluminum content between samples, Al:Ni ratios were derived from SEM-EDS and XRF. To obtain Al:Ni ratios by SEM-EDS, between 20 and 100 EDS spectra were measured at multiple positions for each sample (Figures S12−S21 for location of the SEM-EDS point scans). The SEM-EDS Al:Ni ratios were then calculated by averaging the values from these spectra. The XRF Al:Ni ratios were obtained directly from a duplicate of the XRF measurement, and they show ratios between 0.012 ± 0.001 and 0.015 ± 0.002 (Table S7) for samples annealed at temperatures up to 500 °C (Figure 3b). The Al:Ni ratios derived from EDS for this temperature range lie between 0.010 ± 0.002 and 0.022 ± 0.002, being generally larger compared with XRF except for the sample annealed at 200 °C. This is not surprising considering that the measurement depth of XRF is larger and so the relative amount of aluminum compared to the bulk that is being analyzed is lower.[50,51] The larger fluctuations in aluminum content between samples seen by EDS are attributed to inhomogeneities in the samples at a microscopic level. At 600 °C, both EDS and XRF show a decrease in aluminum content with XRF measuring an Al:Ni ratio of 0.0079 ± 0.0001 at 600 °C and EDS measuring 0.014 ± 0.001. The aluminum content measured by both techniques decreases further as the annealing temperature increases, reaching comparable values for both techniques at 800 °C of 0.004 ± 0.001 for XRF and 0.0052 ± 0.0009 for EDS (Tables S6 and S7). This strongly suggests that the coating is diffusing into the bulk of the particles beyond the depth of analysis of these techniques. Having proved that the coating process leads to the deposition of a rough layer on the surface of NMC811 and to the presence of aluminum in the particles, the composition of this coating layer was then studied using TEM in STEM modes (Figures S29−S33 and Tables S3−S5). The TEM-EDS maps were measured allowing the aluminum content at the surface coating region (20−100 nm) to be determined, confirming that the aluminum signal seen in SEM-EDS and XRF comes from the deposited layer, which has a much higher aluminum content compared to the bulk (Figure S36). Al:Ni ratios of 0.50 ± 0.07 and 0.40 ± 0.05 were calculated for the 200 and 400 °C samples with a large decrease in aluminum content in the surface regions detected for the 600 and 800 °C (0.02 ± 0.04 and 0.02 ± 0.05) samples.

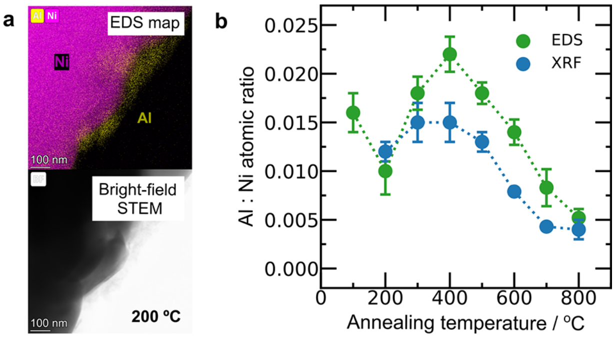

Figure 3. (a) EDS map and STEM image in the bright field mode of the coated NMC811 annealed under air at 200 °C; (b) changes in aluminum to nickel atomic ratio as a function of annealing temperature as determined by EDS and XRF. The error bars are the 95% confidence intervals of measurements taken across several particles. Similar levels of aluminum content are detected up to a 500 °C annealing temperature, but a decrease in aluminum content is seen at higher temperatures. Since both EDS and XRF measure the near-surface composition of the sample, this provides evidence for diffusion of aluminum into the bulk of the particles.

XPS was then performed as a surface-specific technique to understand the composition and chemical environments present and their temperature-induced changes in the coating in more detail. High-resolution XPS spectra of the aluminum 2p region contain peaks corresponding to the transition metals (Ni, Co, Mn), lithium, and aluminum (Figure 4). This region was hence fitted to eight components (Al 2p, Mn 3p, Li 1s, Co 3p, Co 3p satellite, Ni $3p_{3/2}$, Ni $3p_{1/2}$, Ni 3p satellite, see Tables S10 and S11 for details on the XPS fittings). Small variations were detected in the binding energies of the nickel, cobalt, and manganese peaks between the samples, which are

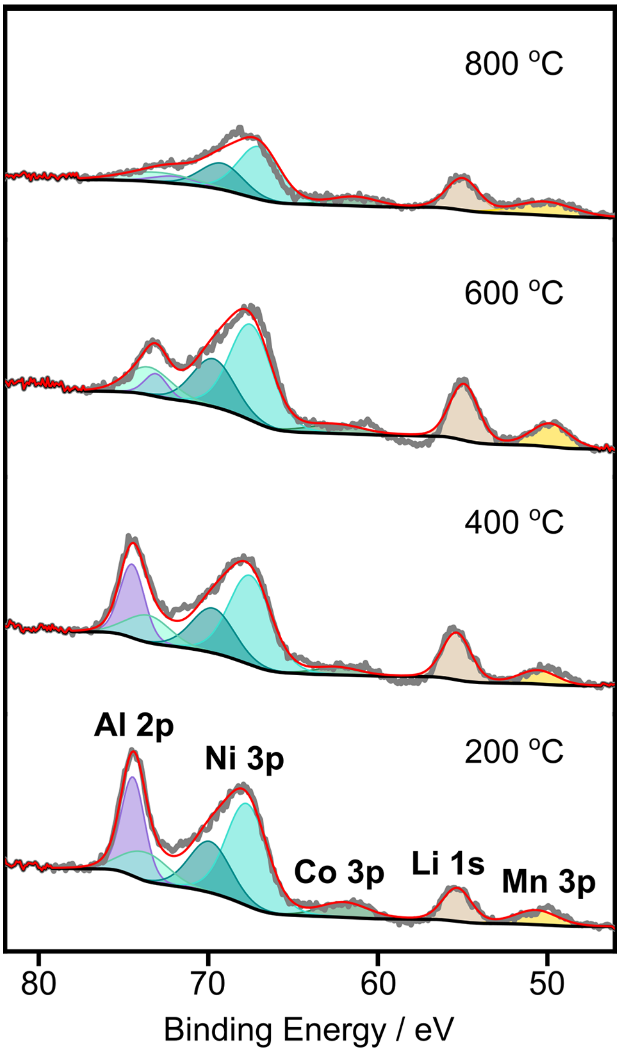

Figure 4. Al 2p region of the XPS spectra of Al_2O_3-coated NMC811 annealed at different temperatures; see Table S10 for the intensities and binding energies obtained by fitting these spectra. The binding energies of the Al 2p peak (purple) support the presence of aluminum oxide. Furthermore, the decrease in intensity of this peak supports the diffusion of the aluminum ions into the bulk of the particles.

likely attributable to imperfect charge correction (the carbon 1s signal arising from surface C−H, C−C was set to 284.8 eV in this work). Such minor variations are typical of powders and complex nonuniform materials, where differential charging can occur.[52] That there are no clear trends or significant changes in the binding energies indicates that the oxidation states of the transition metals on the surface remain the same after coating and annealing.

Relative to the intensities of the peaks corresponding to Ni, Mn, and Co 2p orbitals, the Al 2p peak decreases in intensity with a higher annealing temperature (Figure 4). In contrast, the intensity ratio of the Ni, Mn, and Co 2p peaks remains approximately constant, corresponding to the expected 8:1:1 elemental ratio. This is again consistent with the diffusion of Al from the coating into the bulk of the particles and is mirrored by the lower aluminum contents detected at higher temperatures (600 and 800 °C) from the survey scans. As a result of the lower measurement depth of the XPS measurement (as determined by the inelastic mean free paths of the photoelectrons), the aluminum contents determined by XPS were 2 orders of magnitude higher than those determined by SEM-EDS and XRF and an order of magnitude higher than the TEM-derived values, with Al:Ni ratios of the order of 2.76−2.77 up to 400 °C (Figure 4 and Table S13). Above 400 °C, the Al:Ni ratio decreases sharply to 0.87, decreasing further at 800 °C to 0.14. This again shows that the proposed diffusion process does not occur below 400 °C and that at 600 °C, there is significant diffusion taking place with even greater diffusion at higher temperatures (Table S13).

The binding energy of the main Al 2p peak (74.45 eV) confirms that the material deposited onto the samples annealed at 200 and 400 °C is aluminum oxide.[53] A shift in the aluminum 2p peak to lower binding energies (approximately 73.09 eV) is observed at 600 °C. This binding energy is only an approximation because the overlap with the nickel 3p satellite, which gives rise to a broad peak centered at 73.72 eV (blue), makes it difficult to determine the exact position of the Al 2p peak in this sample. Nevertheless, this value matches well with the Al 2p binding energies that Appapillai *et al.*[54] measured for $LiAlO_2$, suggesting that lithiation of the coating has taken place at 600 °C. Consistent with the XRF and EDS results, most of the aluminum has diffused past the measurement depth of XPS into the NMC at 800 °C. The residual XPS signal could arise from either small amounts of coating that has not diffused into the particles or surface Al-doped NMC phases. Lebens-Higgins *et al.* assigned the Al 2p signal from a $LiNi_{0.8}Al_{0.2}O_2$ (LNA) electrode with a binding energy of 72.7 eV[55] to a doped nickel oxide phase of the form $Li_{1-x}Ni_{1-y}Al_yO_2$, suggesting that the signal from our Al-doped NMC phase would be shifted to lower binding energies compared with Al 2p signal arising from a coating. This would increase the overlap with the Ni 3p peak complicating the XPS analysis of aluminum species in this case.

^{27}Al Solid-State NMR Spectroscopy. ^{27}Al solid-state NMR (SS-NMR) spectroscopy was next performed to examine the local structures in more detail. While ^{27}Al SS-NMR is a useful technique to characterize the local structure, the interpretation of the results can be challenging due to the fact that ^{27}Al ($I = 5/2$) is a quadrupolar nucleus and broad signals are often observed. This, coupled to the small amount of aluminum present in our alumina-coated NMC811 particles, leads to difficulties in extracting accurate structural information. Furthermore, the presence of transition-metal ions Ni^{2+}, Ni^{3+}, and Mn^{4+}, which have unpaired electrons and are therefore paramagnetic, can cause shifts in the aluminum signals *via* the Fermi contact interaction.[35] One way of overcoming these problems is to measure the samples at different magnetic fields: at low magnetic fields, the effects of the paramagnetic ions are minimized, while at high magnetic fields, the second-order quadrupolar interaction is reduced, leading to sharper lines for the ^{27}Al diamagnetic signals.

The ^{27}Al NMR spectra of Al_2O_3-coated NMC811 samples measured on a 700 MHz spectrometer (16.4 T) are shown in Figure 5. Aluminum oxides have three possible coordination environments for the aluminum atom [4-, 5-, and 6-coordinate sites ($^{[4]}$Al, $^{[5]}$Al, and $^{[6]}$Al)] that depend on the number of oxygen atoms coordinating to the aluminum. These environments give rise to distinct resonances with isotropic chemical shifts of approximately $\delta_{iso}(^{[4]}Al) = 60$ ppm, $\delta_{iso}(^{[5]}Al) = 30$ ppm, and $\delta_{iso}(^{[6]}Al) = 0$ ppm,[57] allowing the relative concentration of each site to be determined. No difference in signal intensity in the diamagnetic region is seen on going from an annealing temperature of 200 to 400 °C, but changes in relative intensity at 600 °C are seen and very little signal from diamagnetic species remains by 800 °C, again confirming that the diffusion process starts at temperatures higher than 400 °C.

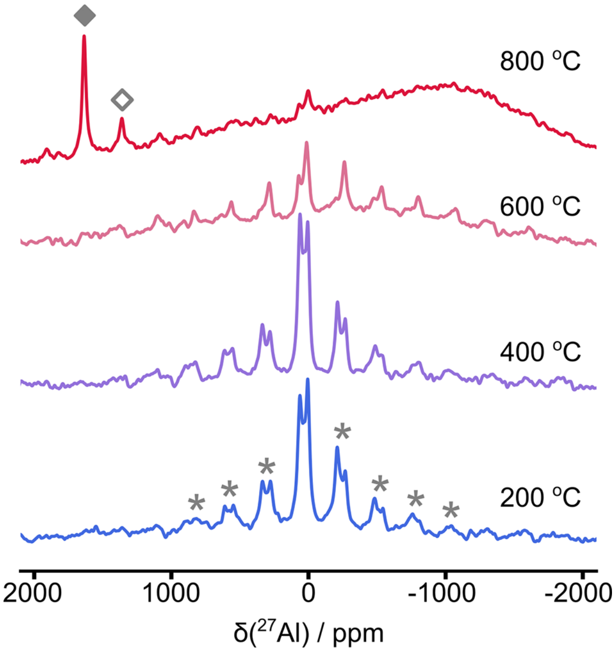

Figure 5. ^{27}Al solid-state NMR spectra of Al_2O_3-coated NMC811 annealed at various temperatures in air, as indicated in the figure. The spectra were recorded at a magnetic field strength of 16.4 T and an MAS frequency of 50 kHz and are scaled by the sample mass and the number of scans acquired. Spinning sidebands are marked with asterisks in the 200 °C spectrum. All samples except the 800 °C sample were as-coated/annealed powders. The 800 °C sample was scraped from an electrode, with the small residues of the aluminum current collector in the sample leading to an aluminum metal signal at 1636 ppm (the isotropic resonance and spinning sideband being marked with filled and empty diamonds, respectively).[56] The intensity of the diamagnetic signal decreases as the annealing temperature is increased, and a broad feature at negative ppm caused by aluminum near transition-metal atoms grows at high annealing temperatures.

A very broad signal centered at approximately −1000 ppm is seen in the spectrum of the 800 °C sample. This signal is assigned to aluminum doped into the transition-metal layer of NMC811, with the shift with respect to the signal from the alumina coating arising from Fermi contact interactions with the paramagnetic transition-metal ions Ni^{2+}, Ni^{3+}, and Mn^{4+}.[35] To confirm this assignment, a spectrum of the same sample was also acquired at a lower magnetic field of 4.7 T (Figure S45). The position of the more clearly resolved ^{27}Al resonance (approximately −1200 ppm) compares well with literature ^{27}Al spectra of NCA ($LiNi_{1-y-z}Co_yAl_zO_2$), confirming that the aluminum observed here is located in the TM layer largely nearby $Ni^{2+/3+}$ ions, with the $Ni^{2+/3+}$ ions in the first cation coordination shell of Al^{3+} giving rise to negative shifts.[58] The presence of some aluminum in the bulk NMC phase is also inferred from the spectrum of the 600 °C sample where a broad signal is observed under the diamagnetic signals (Figure 5). The ^{27}Al SS-NMR spectrum of the sample annealed in oxygen at 800 °C was almost identical to that of the air-annealed sample, confirming migration of most of the Al into the bulk (Figure S46).

Figure 6 shows the central (isotropic) resonances of ^{27}Al SS-NMR spectra measured on a 1 GHz spectrometer, performed at the higher magnetic field (23.5 T) to reduce the second-order quadrupolar interaction and increase the signal-to-noise ratio. The three peaks corresponding to the $^{[4]}Al$, $^{[5]}Al$, and $^{[6]}Al$ environments nearby diamagnetic cations can be identified. There is a significant amount of aluminum in a five-coordinate environment in the 200 and 400 °C samples, which proves that the coating is amorphous, since no crystalline phase of aluminum oxide contains this local environment.[59]

In order to deconvolute the spectra and quantify the amount of $^{[4]}Al$, $^{[5]}Al$, and $^{[6]}Al$ aluminum present in the samples, the NMR spectra were modeled using the Czjzek model[47] for each peak (Figure 6), with the parameters summarized in Table S14. The Czjzek model accounts for the distribution of quadrupolar interactions present in amorphous alumina due to its disordered structure; it describes the distribution of local environments and thus quadrupolar interactions, leading to characteristic NMR signals with tails toward lower ppm values.[47]

The percentages and absolute integrated intensities of the observed signals assigned to the $^{[4]}Al$, $^{[5]}Al$, and $^{[6]}Al$ sites are derived directly from the fit and shown in Figure 7. An increase in $^{[4]}Al$ and $^{[5]}Al$ and a decrease in the $^{[6]}Al$ signals are observed going from 200 to 400 °C. A previous report on temperature-dependent structural evolution of amorphous alumina grown by chemical vapor deposition (CVD) methods also using AIP as a precursor shows an evolution of the aluminum environments with increasing deposition temperatures similar to what we observe.[59] The intensities in the 200 and 400 °C spectra remain comparable, while at 600 °C, a sharp decrease in signal intensity is seen, suggesting that a significant amount of aluminum diffusion has occurred at this temperature.

As the annealing temperature is increased, an increase in crystallinity of the aluminum oxide is normally expected, generally leading to γ-Al_2O_3, a process which should be accompanied by an increase in intensity of the $^{[6]}Al$ signal.[59] Instead, however, an increase in the relative intensity of the $^{[4]}Al$ signal is seen, which is coupled to a marked decrease in $^{[6]}Al$ signal and a slight increase in $^{[5]}Al$ at 400 °C. At 600 °C, the relative intensity of the $^{[4]}Al$ peak increases even further, while the $^{[5]}Al$ and $^{[6]}Al$ environments remain low, with $^{[5]}Al$ decreasing and $^{[6]}Al$ increasing in relative intensity with respect to the 400 °C spectrum. The $^{[4]}Al$ and $^{[6]}Al$ peaks shift from 75 to 82 ppm and from 13 to 19 ppm, respectively (Table S14), supporting the formation of lithiated alumina that contains a large proportion of $^{[4]}Al$.

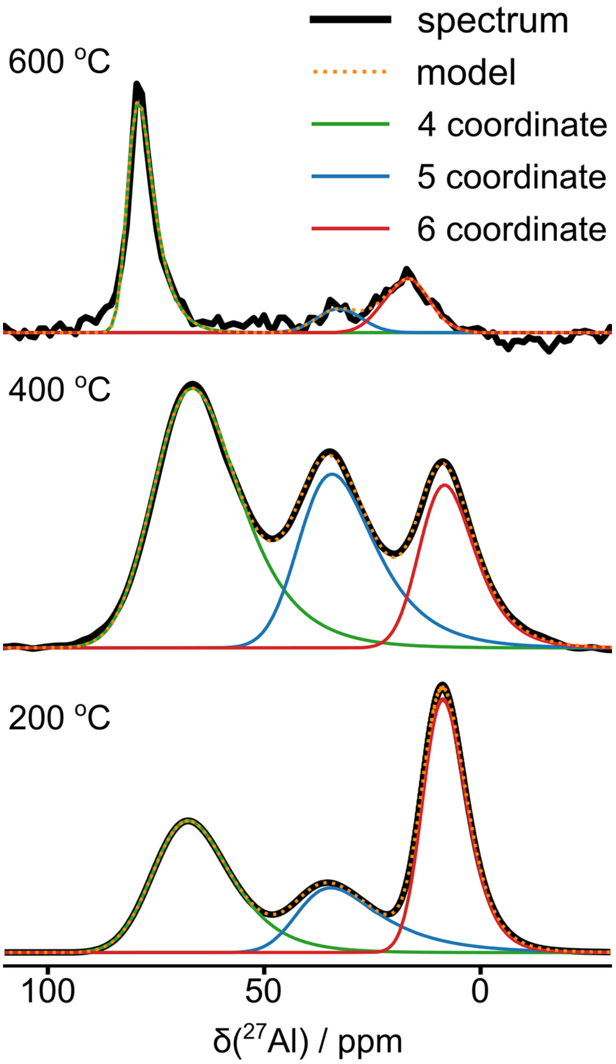

Figure 6. Central resonance of ^{27}Al solid-state NMR spectra (black) of Al_2O_3-coated NMC811 annealed at various temperatures, as indicated in the figure, along with fits applying the Czjzek model (orange dotted line).[47] The three aluminum environments are plotted under the curve and correspond to 4 (green)-, 5 (blue)-, and 6 (red)-coordinated aluminum. The spectra were acquired at 23.5 T and at an MAS frequency of 40 kHz for the samples annealed at 200 and 600 °C and of 38 kHz for the sample annealed at 400 °C.

The low-pressure phase of $LiAlO_2$, γ-$LiAlO_2$, contains tetrahedrally coordinated Al sites and gives rise to shifts between 82 and 80 ppm.[60,61] The monoclinic phase β-$LiAlO_2$ also contains 4-coordinated Al and gives rise to signals at 83 ppm,[60] while the high-pressure phases α-, δ-$LiAlO_2$ contain 6-coordinated Al sites with isotropic shifts of 15−17 ppm.[61] Our results are, therefore, consistent with a disordered/nanoparticulate γ-$LiAlO_2$ phase or an amorphous phase with the local structure similar to that found in γ-$LiAlO_2$ and a small amount of an α-alumina-like phases.[60,61] This formation of lithiated alumina phases after annealing Al_2O_3-coated NMCs

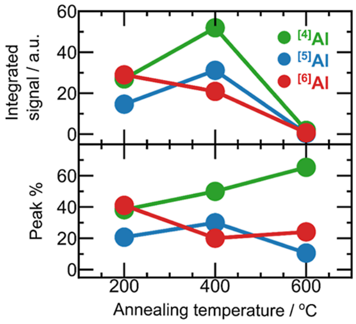

Figure 7. Evolution of the three aluminum coordination environments in the alumina-coated NMC811 particles as a function of annealing temperature as obtained from the simulation of the ^{27}Al SS-NMR spectra shown in Figure 6. The signal integration is shown in the top panel, indicating the evolution of the total quantity of $^{[4]}$Al, $^{[5]}$Al, and $^{[6]}$Al sites in the samples, and the relative distribution of the three alumina sites is shown in the bottom panel.

to higher temperatures has also been observed by others[28,35] and could potentially lead to better lithium conductivity through the coating.

Powder X-ray Diffraction. We next turned to PXRD to determine whether the coating/annealing processes have an effect on the long-range structure of the material (with patterns and refinements reported in Figures S47−S53 and Tables S15−S22). Pristine samples and coated samples annealed at 200, 500, and 800 °C were compared with a coated sample annealed under oxygen at 800 °C and with an uncoated sample annealed under air at 400 and 800 °C. For all these samples, except for the coated NMC annealed under air at 800 °C, Rietveld refinement shows that the reflections can be indexed to a single $R\bar{3}m$ phase with no significant differences in the lattice parameters. The degree of anti-site mixing was also similar, increasing at higher annealing temperatures for both the coated and uncoated samples. This matches well with the ^{7}Li SS-NMR measurements carried out at 4.7 T (Figure S44) in which no significant changes were seen between samples, suggesting that the bulk did not change considerably after the coating and annealing processes up to 500 °C. However, the coated sample annealed under air at 800 °C shows a splitting of the 003, 101, and 104 reflections, and the XRD pattern could not be fit to a single phase (Figure S50). The introduction of the secondary aluminum-doped NMC811 phase with a larger c lattice parameter (14.3845 Å *vs* 14.2457 Å) in which Al^{3+} ions substitute into the transition-metal sites[32] gave a good agreement with the measured data. The amount of this secondary phase was estimated to be 5% of the total in the material, suggesting that this new phase is likely a near-surface modification and that the bulk of the NMC remains intact. No preference for substitution of a specific transition metal (cobalt, nickel, or manganese) by aluminum could be identified by PXRD due to the similar scattering factors of the transition metals.

No significant changes in (bulk) lattice parameters were observed for any of the control samples or the oxygen-annealed sample. An increase in cation mixing was seen after annealing under air at 800 °C, with or without the coating, indicating that annealing under air at 800 °C has, in itself, an effect on the structure of the material. The degree of mixing could be reduced by annealing under oxygen at 800 °C (3.2% *vs* 4.5% for O_2 *vs* air, respectively), with the O_2-annealed sample showing no evidence of a secondary phase. Annealing at 400 °C under air did not lead to an increase in cation mixing.

Electrochemistry. The next step involved an investigation of how the coatings affect the electrochemical properties of the NMC811 cathode and whether coatings or surface doping increases the capacity retention of the material. For this, galvanostatic cycling was performed for the coated and uncoated materials using a half-cell configuration (Figures 8, 9, S54, and S55 and Tables S23 and S24). Cells were cycled between 3.0 and 4.3 V at C/2 for 250 cycles. The upper cutoff voltage of 4.3 V was chosen since cycling above 4.2 V results in more aggressive battery degradation.[4] Two slow cycles at C/20 were included every 50 cycles to assess if the observed capacity loss was intrinsic to the material or caused by slow kinetics.

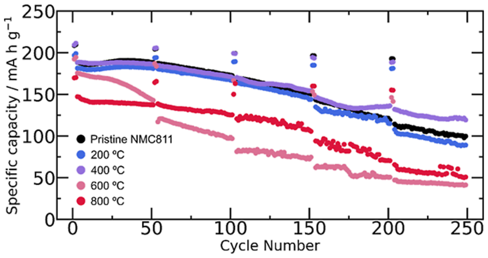

Figure 8. Selected long-term cycling data. After two formation cycles at C/20, the cells were cycled at C/2 between 3.0 and 4.3 V, with two slow cycles at C/20 every 50 cycles. Similar discharge capacities and capacity fade are observed for the pristine NMC811 and the coated samples up to 400 °C, while lower capacities are observed at higher annealing temperatures.

The control (uncoated) sample annealed at 400 °C has similar initial capacities compared to the pristine NMC811, with an average of 186 and 179.9 mA h g^{-1} at C/2 and 206 and 199.9 mA h g^{-1} at C/20 for the pristine and control samples, respectively (Figure S55a and Table S23). However, the control sample has a better capacity retention than the pristine material at C/2 current rates after 200 cycles (19.7% less C/2 capacity loss, Table S23), suggesting that washing with dry toluene and heating to 400 °C under air have a beneficial effect on the capacity retention. In contrast to the 400 °C control sample, the 800 °C control sample showed a substantial decrease in initial capacity, both at C/2 (30.9 less mA h g^{-1}) and at C/20 (29.6 less mA h g^{-1}), which could result from the 2.9% increase in Ni occupancy in the Li layer seen between control samples annealed at 400 and 800 °C under air (Tables S20 and S21).[62] Nevertheless, better capacity retention than the pristine NMC811 (4.5% less capacity loss at C/2) is still observed for this sample, again consistent with the idea that the coating process in itself (rather than the coating per se) results in better capacity retention (See Table S24 for full data on the initial specific capacities and capacity loss of the 800 °C annealed samples). These improvements could be caused by the washing step, or by the heating, as it has been shown that Li_2CO_3 decomposes forming CO_2 at temperatures below 400 °C for NMC811.[63]

Having studied the effect of the solvent treatment and annealing on uncoated particles, we then studied the effect of the coating on the electrochemistry of the material. The pristine NMC811 was compared to the as-coated sample and the coated samples annealed under air at 200−600 °C and 800 °C. Electrochemical testing of the 700 °C sample was inconclusive due to the much faster degradation observed for this sample, possibly in part due to the lower amount of active material (approximately 50% less), meaning that it was difficult to produce good films for the electrochemistry, and the results are therefore not reported here. A selection of the specific capacity versus cycle data is shown in Figure 8 (see Figures S54 and S55 and Tables S23 and S24 for the full data).

The pristine NMC and the samples annealed at 200 and 400 °C show similar initial discharge capacities ranging between 188.5 and 181.4 mA h g^{-1} at C/2. The sample annealed at 600 °C has a slightly lower initial capacity of 175.5 mA h g^{-1}, while the sample annealed at 800 °C presents a significantly lower initial capacity of 147.3 mA h g^{-1}. The rate of capacity fade also changes as a function of annealing temperature. At slow rates (C/20), the capacity fade is similar for the pristine NMC811 and for the coated electrodes annealed at 200 and 400 °C, while at faster rates (C/2), the coated sample annealed at 400 °C shows similar capacity retention to the 400 °C control sample, with slightly better capacity retention compared to the pristine sample which loses 47% of its specific discharge capacity after 250 cycles and samples annealed at 200 and 400 °C losing 50 and 37% of their capacity, respectively. The samples annealed at higher temperatures show noticeably lower capacity retentions, with the samples annealed at 600 and 800 °C losing 77 and 66% of their C/2 specific discharge capacity, respectively. Furthermore, the fade rate seems to be accelerated substantially after 25 cycles in the samples annealed at 600 °C, while for the samples annealed at 800 °C, there is a more gradual decay. The capacity of the 800 °C sample fades at a similar rate to the pristine sample up to cycle 150, at which point it starts degrading faster than the pristine sample. The rapid degradation even at slow rates for the 600 °C sample is tentatively ascribed to the formation of a more crystalline, γ-$LiAlO_2$-like coating phase at this temperature, as seen in the SS-NMR spectra. Crystalline γ-$LiAlO_2$ phase is a poor Li^+ conductor,[61] and given the coating thicknesses of 19−34 nm observed by TEM, we suggest that transport through the poorly conducting phase impacts capacity. Furthermore, the fact that the surface morphology becomes rougher at this temperature may also have an effect on the capacity retention by increasing the surface area and possibly promoting electrolyte degradation.

By comparison with the uncoated sample annealed at 800 °C, it is clear that the poor capacity and capacity retention observed for the coated sample annealed at 800 °C cannot be attributed only to the heating under air and that the Al doping has a negative effect on the material's initial capacity and capacity retention (this is nearly 10 mA h g^{-1} less initial capacity at C/2 and C/20 for the coated material and 22.7% more capacity loss at C/2 after 200 cycles for the coated *vs* Noncoated materials annealed in air at 800 °C). The fact that the coated sample annealed at 800 °C shows less capacity retention than the pristine sample at (C/2) rates but not at (C/20) suggests that the capacity loss observed at high rates is a kinetic effect. This is surprising, given that at this temperature, a large fraction of the Al^+ ions have diffused into the particles, but it may be associated with the secondary phase seen by XRD.

To test if better capacity retention can be accessed by annealing under oxygen, a coated sample annealed under oxygen at 800 °C was synthesized. The PXRD results (Figure S53 and Table S22) now showed no secondary phases. Furthermore, less cation mixing was found compared to the sample annealed at 800 °C under air (3.2% of Ni in Li sites for the O_2-annealed sample and 4.5% for the air-annealed sample). Electrochemically, this sample shows higher initial capacities compared to the sample annealed at 800 °C under air (21.4−26.5 mA h g^{-1} difference) (Figure S55 and Table S24), which is attributed to the lower amount of cation mixing and possibly the lack of a secondary phase. It shows similar rates of degradation compared to the air-annealed sample at C/2 but faster degradation at C/20 (10% more degradation for the sample annealed under O_2).

Given the very different electrochemical performances of the samples annealed at 400, 600, and 800 °C, we then investigated the samples annealed using smaller temperature steps of 100 °C. The voltage profiles and their corresponding $dQdV^{-1}$ plots are plotted in Figure 9. Since there are only small differences in the $dQdV^{-1}$ profiles of the pristine sample and the samples annealed between 100 and 300 °C, only the samples annealed at 400 to 800 °C are compared in this figure. The decrease in specific capacities is negligible in cycle 2 for the 200 and 400 °C samples and small for samples annealed from 500 °C up to 600 °C, but a much larger decrease in specific capacity is seen for the sample annealed at 800 °C. By cycle 203, the poor performance of the 600 °C sample is clearly visible, with even poorer performance seen for the 600 °C sample along with a partial recovery in capacity for the 800 °C sample.

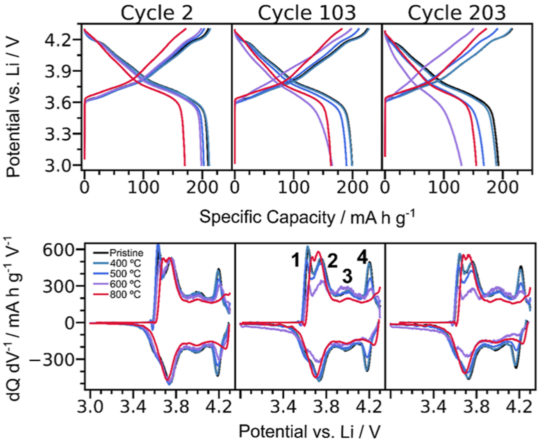

Figure 9. Voltage profiles and $dQdV^{-1}$*vs* voltage for half cells made with pristine NMC811 or Al_2O_3-coated NMC811 annealed at different temperatures. Cycles 2 (left), 103 (middle), and 203 (right) are shown, which were all performed at C/20.

The slow cycle rate data (C/20) were used to carry out the $dQdV^{-1}$ analysis and to separate the different electrochemical features and minimize impedance effects on the observed profiles. All samples show four peaks (labeled 1−4) on charge and discharge in their $dQdV^{-1}$ as expected for NMC811.[64] The $dQdV^{-1}$ profiles are quite symmetric between charge and discharge in cycle 2, showing good reversibility of the charge/discharge cycle. Peak 4, which is associated with the flatter voltage process at close to 4.2 V, shifts to higher voltages on charge and decreases in intensity as the annealing temperature increases, especially at 800 °C, where it almost vanishes. It is particularly clear from the $dQdV^{-1}$ plot of cycle 2 that much of the loss in capacity comes from the capacity associated with peak 4. This trend is also observed at higher cycle numbers. This peak is only observed in the nickel-rich NMCs and LNO and has been associated with lattice collapse which occurs for NMC materials at high states of charge. It is at and above this voltage where much of the degradation is observed.[65] Interestingly, the sample annealed at 800 °C shows a recovery of capacity retention and a partial merging of peaks 1 and 2 in its dQdV^{-1}.

Post-Mortem Analysis. To understand the evolution of the coating with cycling, SEM-EDS, TEM, and STEM-EDS of the coated materials annealed at 200 and 400 °C after 250 or 300 cycles in half cells were measured. SEM showed the presence of decomposed material (containing fluorine) and fragments of the glass fiber separator on the surface, which made it difficult to characterize the surface morphology in this material. Less closely attached primary particles compared to the pristine samples are seen in both SEM and TEM. SEM-EDS shows similar Al:Ni ratios after electrochemical cycling, while TEM shows lower Al:Ni ratios. Furthermore, less coated regions and thinner coatings were found using TEM after electrochemical cycling, suggesting that thicker regions of the coating can delaminate or detach after extensive cycling or undergo chemical reaction during cycling (Tables S2 and S6 and Figures S20, S21, S27, S28, and S34−S36).

■ DISCUSSION

We now discuss the differences in the electrochemical cycling behavior in the context of the structures of the alumina coatings and Al^{3+} migration achieved with our coating method and *via* previous approaches. All characterization data obtained here for the sample annealed at 800 °C are consistent with diffusion of Al^{3+} into the bulk NMC phase and the formation of a secondary phase with a larger lattice *c*-parameter. Dogan and co-workers have also observed a ^{27}Al NMR signal from aluminum nuclei nearby paramagnetic ions in Al_2O_3-coated NMC811 annealed at 800 °C,[35] consistent with Al^{3+} incorporation into the bulk. In this earlier work, the aluminum oxide coating was deposited by evaporation of an aqueous $Al(NO_3)_3$ solution at 80 °C.[35] We observed a broad peak centered around −1200 ppm with a linewidth of more than 600 ppm at 4.7 T (Figure S45) at a peak position close to that seen for NCA samples with composition $LiNi_{0.8}Co_{0.15}Al_{0.05}O_2$ and on that basis assigned this peak to a local environment nearby predominantly $Ni^{2+/3+}$.[58,66] In contrast, the earlier work observed an even broader signal with discrete resonances at less negative ppm values (between 0 and 1000 ppm), with the peaks being assigned to local environments containing more Co^{3+} ions in their local coordination shells.[35] The presence of these environments was ascribed to Co segregation at the surface of the NMC811 particles in the pristine material. However, we see no evidence for Co^{3+} segregation in the NMC811 sample used in our work. Small amounts of $^{[4]}$Al, $^{[5]}$Al, and $^{[6]}$Al were also detected after heat treatment at 800 °C in the earlier study[35] where the $^{[4]}$Al peak was observed at 69 ppm and thus cannot be assigned to crystalline γ-$LiAlO_2$ ($^{[4]}$Al peak at 80−82 ppm).[60] On the other hand, this shift is higher in ppm than expected for $^{[4]}$Al in Al_2O_3,[57,67] and in the previous work, the authors assigned the peak to γ-$LiAlO_2$ at grain boundaries.[35] The residual diamagnetic species likely arise from the higher wt % Al contents of their films and the coating method, which likely leads to less uniform deposition. Finally, we note that a distinct second Al-rich phase with larger cell parameters ($a = b = 2.88$ Å and $c = 14.25$ Å *vs* $a = b = 2.89$ Å and $c = 14.38$ Å for the expanded phase) was seen in our work. Previous coating studies reported a single phase and only an increase in unit cell volume after annealing at 800 °C for Al_2O_3-coated LCO and NMC532 in one report[41] and NMC622 and 811 in another (this study seeing additional peaks that were ascribed to stacking faults at high Al contents[35]). This behavior may be due to the lower solubility of Al in high nickel-content materials.[35] Furthermore, this secondary phase does not form on annealing in oxygen.

In their Al_2O_3 coatings of NMC532, 622, and 811 annealed at 400 °C, Dogan and co-workers observed a broad peak between 0 and approximately 25 ppm that was assigned to $^{[6]}$Al in an Al_2O_3 phase or α-$LiAlO_2$.[35] Their ^{27}Al NMR spectra are very different from those observed in our work, where the large fraction of aluminum ions in $^{[4]}$Al and $^{[5]}$Al sites indicates the amorphous nature of our coatings. Typical amorphous alumina materials contain peaks at approx. 0 ppm for $^{[6]}$Al, 30 ppm for $^{[5]}$Al, and 60 ppm for $^{[4]}$Al.[57,67] Furthermore, amorphous alumina generally reacts first to form a γ-Al_2O_3-like phase, which contains both $^{[6]}$Al and $^{[4]}$Al, and much higher temperatures are required to form crystalline phases such as α-Al_2O_3, which are formed of octahedrally coordinated aluminum sites only. This suggests that the coatings that form in wet coating methods, and that likely contain $^{[6]}$Al ions coordinated to hydroxyl groups and water molecules before drying, evolve differently on annealing. Perhaps more surprisingly, the same researchers observed only $^{[6]}$Al environments in coatings prepared when using 2 wt % AIP dissolved in either xylene or methanol as a solvent and annealed at 400 °C,[42] albeit on NMC532, suggesting perhaps that the removal of excess AIP (as in our method) may also be important in controlling the evolution of the Al^{3+} environments within the coatings.

Our results show the presence of γ-$LiAlO_2$-like local environments in the sample annealed at 600 °C. Although the reaction of the Al_2O_3 coating with surface impurities such as Li_2CO_3 and LiOH will contribute to an extent to the formation of $LiAlO_2$, it is unlikely that these impurities would provide enough lithium for the conversion of Al_2O_3 into $LiAlO_2$ on their own. On the other hand, previous reports suggest that Al_2O_3 coating under a variety of conditions leads to the extraction of bulk Li^+ from NMCs to form $LiAlO_2$ after an annealing step.[41,42] Furthermore, the evidence presented in this work of diffusion of the coating into the bulk of the NMC suggests that diffusion of Li^+ from the bulk into the coating also occurs. If this lithiation of the coating proceeds by delithiation of the NMC, there are at least two possible reaction pathways

$$x Al_2O_3 + LiMO_2 + x/2\ O_2 \rightarrow 2x\ LiAlO_2 + Li_{(1-2x)}MO_2 \tag{1}$$

$$x Al_2O_3 + LiMO_2 \rightarrow 2x\ LiAlO_2 + Li_{(1-2x)}MO_{(2-x)} \tag{2}$$

The NMC could be oxidized (eq 1) or densified at this high annealing temperatures (eq 2). While the lithium removal from the NMC bulk (eq 1) might explain any lower capacity of a sample on the first charge, it should not result in a decrease in capacity on discharging in a half cell. Furthermore, XPS provides no clear evidence for any change of oxidation state of the transition-metal ions. Thus, the reaction likely occurs *via*eq 2, but reactions with surface lithium carbonates may also occur in this temperature regime, providing another source of Li^+. Annealing in O_2 may favor reaction 1, perhaps explaining why no secondary phase is seen on annealing at 800 °C in O_2. This work highlights the fact that different coating conditions (solvents, precursor, wt % of precursor, reaction times, atmosphere, temperatures, and the surface chemistry of the substrate) can have a noticeable effect on the structure of the resultant coating and its degree of crystallinity.

The electrochemical trends can be partially explained by considering the insulating nature of the coating and the electrochemistry of aluminum-doped NMC phases. The coating is an electronic and ionic insulator and may hinder the extraction/insertion of lithium ions during the first charge/discharge. However, the NMC811 electrodes with amorphous coatings formed on annealing at 200 and 400 °C show good electrochemical performance at both high and low rates, with the 400 °C coating process resulting in marginally improved capacity retention over the uncoated at higher rates. This suggests that the amorphous alumina coating is better able to support Li^+ transport through it. By comparison, the AIP coatings formed in MeOH and xylene in earlier work at the same temperature, which contained $^{[6]}Al$ only, were associated with poor capacity retention.[42] We note, however, that these results were obtained for NMC532, and the materials were cycled to 4.5 V, with a higher voltage being needed to extract a similar amount of Li.

The worst electrochemical performance is seen for 600 °C at both low and high rates. The fact that capacity at both high and low rates is only slightly worse than that of the uncoated electrode in the first 20 cycles further supports the idea that the $LiAlO_2$ formation alone does not cause the faster capacity fade at 600 °C. The 600 °C particle surfaces are rougher and the primary particles appear more distinct in the SEM images (Figure 2), and this morphology change may be associated with the γ-$LiAlO_2$ crystallization process. One hypothesis, which requires further experiments to confirm, is that the morphological changes may promote more electrolyte degradation reactions and possibly more mechanical degradation. What is clear is that the γ-$LiAlO_2$-like coating formed here does not prevent a significant growth in the Ohmic resistance during cycling.

When the aluminum from $LiAlO_2$ has been incorporated into the transition-metal layers, a recovery in the capacity retention is observed at low cycling rates, and both pristine NMC811 and the sample annealed at 800 °C in air retain 91−92% of their initial C/20 capacity after 203 cycles. The drop in the first and second capacity retention can be ascribed to Al substitution as the aluminum-doped NMC phase will have lower capacities than the pristine NMC because aluminum is electrochemically inactive. This is consistent with essentially all the literature on NMC alumina-coated samples heated to 800 °C.[32,35] However, the Al substitution into the bulk and the formation of a second phase (as seen by XRD) again do not prevent the gradual increase in Ohmic resistance and reduced capacity seen at higher rates with cycle number, also consistent with prior work.[35] This suggests that Al^{3+} substitution into the bulk does little to reduce the extent of rock-salt formation in these high-nickel materials, which is one source of NMC degradation.[20]

Finally, we should compare our coating method to that of Neudeck *et al.*,[8] who saw an improvement in capacity retention after coating wet (1000−1200 ppm of water) NMC811 with TMA in toluene, removing the unreacted precursor before drying, but with no annealing step. Neudeck *et al.* tested their material in full (NMC811/graphite) pouch cells at 1C cycling rate and 45 °C and obtained impressive behavior, extending the lifetimes of their batteries from 600 to over 1100 cycles (based on an 80% capacity retention). They speculate that their process removes water from the surface of the NMCs, improving capacity retention. Their coating must similarly be amorphous, and their work motivates further studies of our 200 and 400 °C annealed samples in full cells. More recent work on TMA coatings on $Li(Ni_{0.70}Co_{0.15}Mn_{0.15})O_2$ by Negi *et al.* has also seen good performance for amorphous alumina coatings, but they see improved performance for a mixed amorphous $Al_2O_3/LiAlO_2$ coating layer, which they ascribed to increased lithium-ion conductivity.[28] These authors similarly use NMR to characterize their coatings, and the broadness of their ^{27}Al signals is consistent with an amorphous coating and the formation of $LiAlO_2$ at 600 °C.

■ CONCLUSIONS

Although alumina coatings have been shown to increase the lifetime of a range of lower-nickel content NMCs, their efficacy for Ni-rich materials such as NMC811 is less clear with various studies producing contradictory results. Since this could be a consequence of the different coating methods used in these studies, which result in different phases and uniformity of the alumina coatings, we developed a new wet-chemistry method to deposit alumina on NMC811. The result was a 30−100 nm thick coating, whose structure and electrochemistry were explored as a function of annealing temperature. High-field solid-state NMR spectroscopy, supported by XPS and microscopy, was used to track the development of the alumina coating with temperature, with an amorphous alumina-like coating being seen at low temperatures and a γ-lithium aluminate-like coating at 600 °C. Essentially, all the Al migrated into the bulk on annealing at 800 °C. This evolution differs from a previous report on alumina coating of NMC811, albeit using a different wet-chemistry coating method, which found the presence of $^{[6]}Al$ environments at lower annealing temperatures, assigned to $Al(OH)_6$ or α-$LiAlO_2$, and the presence of $^{[4]}Al$ environments with lower-frequency ^{27}Al NMR shifts than found in γ-$LiAlO_2$ at 800 °C, which they tentatively assigned to environments in grain boundaries.[35]

The electrochemical findings were linked to the evolution of the coating induced by the annealing step by identifying the critical temperature at which doping of aluminum ions occurs in NMC811 and comparing samples that were not coated but still underwent the same annealing and washing steps. Annealing at 200−400 °C resulted in similar capacity fade to pristine NMC811 on cycling the coated NMC materials in half cells to 4.3 V, with the washing and annealing steps but without the coating, yielding similar results. Higher annealing temperatures led to faster degradation in half cells, with annealing at 600 °C, resulting in the greatest capacity fade. Interestingly, the degradation at 800 °C was slower than at 600 °C, but the overall capacity was reduced. This work highlights the need to control the whole coating processes and suggests that alumina coatings do little to prevent degradation in half cells, motivating further studies of full cells and the role that coatings play in cross-over phenomena. Overall, our study provides fundamental information which should be of value in the development and analysis of NMC811 coatings. Future studies in this area will be focused on the exploration of bimetallic alumina coatings with better lithium-ion conductivity and on the evaluation of these materials in full cells.

■ ASSOCIATED CONTENT

Supporting Information

The Supporting Information is available free of charge at https://pubs.acs.org/doi/10.1021/acs.chemmater.2c02580.

> Powder XRD patterns and corresponding Rietveld refinement details; high-resolution SEM and TEM images; details of the SEM/TEM-EDS and XRF analysis; further ^{7}Li and ^{27}Al SS-NMR data and parameters for the Czjzek fittings; details of the XPS measurements including calibration and fittings; and long-term galvanostatic cycling and dQdV^{-1} analyses (PDF)

■ AUTHOR INFORMATION

Corresponding Author

Clare P. Grey − *Yusuf Hamied Department of Chemistry, University of Cambridge, Cambridge CB2 1EW, U.K.; The Faraday Institution, Quad One, Harwell Science and Innovation Campus, Didcot OX11 0RA, U.K.*; orcid.org/0000-0001-5572-192X; Email: cpg27@cam.ac.uk

Authors

Víctor Riesgo-González − *Yusuf Hamied Department of Chemistry, University of Cambridge, Cambridge CB2 1EW, U.K.; The Faraday Institution, Quad One, Harwell Science and Innovation Campus, Didcot OX11 0RA, U.K.*; orcid.org/0000-0002-2433-8562

David S. Hall − *Yusuf Hamied Department of Chemistry, University of Cambridge, Cambridge CB2 1EW, U.K.; The Faraday Institution, Quad One, Harwell Science and Innovation Campus, Didcot OX11 0RA, U.K.*; orcid.org/0000-0001-9632-0399

Katharina Märker − *Yusuf Hamied Department of Chemistry, University of Cambridge, Cambridge CB2 1EW, U.K.; The Faraday Institution, Quad One, Harwell Science and Innovation Campus, Didcot OX11 0RA, U.K.*; orcid.org/0000-0002-5056-7174

Jonathan Slaughter − *Yusuf Hamied Department of Chemistry, University of Cambridge, Cambridge CB2 1EW, U.K.; The Faraday Institution, Quad One, Harwell Science and Innovation Campus, Didcot OX11 0RA, U.K.*; orcid.org/0000-0002-6401-8547

Dominic S. Wright − *Yusuf Hamied Department of Chemistry, University of Cambridge, Cambridge CB2 1EW, U.K.; The Faraday Institution, Quad One, Harwell Science and Innovation Campus, Didcot OX11 0RA, U.K.*; orcid.org/0000-0002-9952-3877

Complete contact information is available at: https://pubs.acs.org/10.1021/acs.chemmater.2c02580

Author Contributions

The manuscript was written through contributions of all authors. V.R.-G., D.S.H., and K.M. designed the study and performed the research. V.R.-G. performed the synthesis, SEM, TEM, EDS, PXRD, XRF, and electrochemical measurements and analyzed the data. K.M. and V.R.-G. performed the NMR experiments and analyzed the data. D.S.H. and V.R.-G. carried out the XPS measurements and analyzed the data. J.S. analyzed data and helped writing the paper. D.S.W. and C.P.G. conceived the idea of the study and analyzed data. All authors have given approval to the final version of the manuscript.

Notes

The authors declare no competing financial interest.

■ ACKNOWLEDGMENTS

This work was supported by the Faraday Institution Degradation Project (grant no. FIRG001 and FIRG024). The authors thank the University of Warwick High-Field NMR Facility and Dr. Dinu Iuga for help with the 1 GHz NMR measurements and the Department of Chemistry at University College London for assistance with the XRF measurements. Thermo Scientific (FEI) Talos F200X G2 TEM was funded through the EPSRC Underpinning Multi-User Equipment Call (EP/P030467/1). The authors acknowledge the use of the Cambridge XPS System, part of Sir Henry Royce Institute—Cambridge Equipment, EPSRC Grant EP/P024947/1.

■ REFERENCES

(1) Whittingham, M. S. Lithium Batteries and Cathode Materials. *Chem. Rev.* **2004**, *104*, 4271−4302.

(2) Li, W.; Erickson, E. M.; Manthiram, A. High-Nickel Layered Oxide Cathodes for Lithium-Based Automotive Batteries. *Nat. Energy* **2020**, *5*, 26−34.

(3) Noh, H.-J.; Youn, S.; Yoon, C. S.; Sun, Y.-K. Comparison of the Structural and Electrochemical Properties of Layered Li[$Ni_xCo_yMn_z$]-O_2 (x = 1/3, 0.5, 0.6, 0.7, 0.8 and 0.85) Cathode Material for Lithium-Ion Batteries. *J. Power Sources* **2013**, *233*, 121−130.

(4) Dose, W. M.; Xu, C.; Grey, C. P.; De Volder, M. F. L. Effect of Anode Slippage on Cathode Cutoff Potential and Degradation Mechanisms in Ni-Rich Li-Ion Batteries. *Cell Rep. Phys. Sci.* **2020**, *1*, 100253.

(5) Jung, R.; Metzger, M.; Maglia, F.; Stinner, C.; Gasteiger, H. A. Oxygen Release and Its Effect on the Cycling Stability of $LiNi_x Mn_y Co_z O_2$ (NMC) Cathode Materials for Li-Ion Batteries. *J. Electrochem. Soc.* **2017**, *164*, A1361−A1377.

(6) Eldesoky, A.; Logan, E. R.; Louli, A. J.; Song, W.; Weber, R.; Hy, S.; Petibon, R.; Harlow, J. E.; Azam, S.; Zsoldos, E.; Dahn, J. R. Impact of Graphite Materials on the Lifetime of NMC811/Graphite Pouch Cells: Part II. Long-Term Cycling, Stack Pressure Growth, Isothermal Microcalorimetry, and Lifetime Projection. *J. Electrochem. Soc.* **2022**, *169*, 010501.

(7) Negi, R. S.; Culver, S. P.; Mazilkin, A.; Brezesinski, T.; Elm, M. T. Enhancing the Electrochemical Performance of Li-$Ni_{0.70}Co_{0.15}Mn_{0.15}O_2$ Cathodes Using a Practical Solution-Based Al 2 O 3 Coating. *ACS Appl. Mater. Interfaces* **2020**, *12*, 31392.

(8) Neudeck, S.; Strauss, F.; Garcia, G.; Wolf, H.; Janek, J.; Hartmann, P.; Brezesinski, T. Room Temperature, Liquid-Phase Al_2O_3 Surface Coating Approach for Ni-Rich Layered Oxide Cathode. *Mater. Chem. Commun.* **2019**, *55*, 2174−2177.

(9) Myung, S.-T.; Izumi, K.; Komaba, S.; Sun, Y.-K.; Yashiro, H.; Kumagai, N. Role of Alumina Coating on Li−Ni−Co−Mn−O Particles as Positive Electrode Material for Lithium-Ion Batteries. *Chem. Mater.* **2005**, *17*, 3695−3704.

(10) Cho, W.; Kim, S.-M.; Song, J. H.; Yim, T.; Woo, S.-G.; Lee, K.-W.; Kim, J.-S.; Kim, Y.-J. Improved Electrochemical and Thermal Properties of Nickel Rich $LiNi_{0.6}Co_{0.2}Mn_{0.2}O_2$ Cathode Materials by SiO_2 Coating. *J. Power Sources* **2015**, *282*, 45−50.

(11) Wang, Z.; Liu, E.; He, C.; Shi, C.; Li, J.; Zhao, N. Effect of Amorphous $FePO_4$ Coating on Structure and Electrochemical Performance of $Li_{1.2}Ni_{0.13}Co_{0.13}Mn_{0.54}O_2$ as Cathode Material for Li-Ion Batteries. *J. Power Sources* **2013**, *236*, 25−32.

(12) Sun, Y.-K.; Lee, M.-J.; Yoon, C. S.; Hassoun, J.; Amine, K.; Scrosati, B. The Role of AlF_3 Coatings in Improving Electrochemical Cycling of Li-Enriched Nickel-Manganese Oxide Electrodes for Li-Ion Batteries. *Adv. Mater.* **2012**, *24*, 1192−1196.

(13) Xie, J.; Sendek, A. D.; Cubuk, E. D.; Zhang, X.; Lu, Z.; Gong, Y.; Wu, T.; Shi, F.; Liu, W.; Reed, E. J.; Cui, Y. Atomic Layer

Deposition of Stable $LiAlF_4$ Lithium Ion Conductive Interfacial Layer for Stable Cathode Cycling. *ACS Nano* **2017**, *11*, 7019−7027.

(14) Shi, Y.; Zhang, M.; Qian, D.; Meng, Y. S. Ultrathin Al_2O_3 Coatings for Improved Cycling Performance and Thermal Stability of $LiNi_{0.5}Co_{0.2}Mn_{0.3}O_2$ Cathode Material. *Electrochim. Acta* **2016**, *203*, 154−161.

(15) Cho, J.; Kim, T.-J.; Kim, Y. J.; Park, B. High-Performance ZrO_2-Coated $LiNiO_2$ Cathode. *Mater. Electrochem. Solid State Lett.* **2001**, *4*, A159−A161.

(16) Beltrop, K.; Klein, S.; Nölle, R.; Wilken, A.; Lee, J. J.; Köster, T. K.-J.; Reiter, J.; Tao, L.; Liang, C.; Winter, M.; Qi, X.; Placke, T. Triphenylphosphine Oxide as Highly Effective Electrolyte Additive for Graphite/NMC811 Lithium Ion Cells. *Chem. Mater.* **2018**, *30*, 2726−2741.

(17) Li, J.; Liu, H.; Xia, J.; Cameron, A. R.; Nie, M.; Botton, G. A.; Dahn, J. R. The Impact of Electrolyte Additives and Upper Cut-off Voltage on the Formation of a Rocksalt Surface Layer in $LiNi_{0.8}Mn_{0.1}Co_{0.1}O_2$ Electrodes. *J. Electrochem. Soc.* **2017**, *164*, A655−A665.

(18) Li, J.; Downie, L. E.; Ma, L.; Qiu, W.; Dahn, J. R. Study of the Failure Mechanisms of $LiNi_{0.8}Mn_{0.1}$ $Co_{0.1}O_2$ Cathode Material for Lithium Ion Batteries. *J. Electrochem. Soc.* **2015**, *162*, A1401−A1408.

(19) Jung, S.-K.; Gwon, H.; Hong, J.; Park, K.-Y.; Seo, D.-H.; Kim, H.; Hyun, J.; Yang, W.; Kang, K. Understanding the Degradation Mechanisms of $LiNi_{0.5}Co_{0.2}Mn_{0.3}O_2$ Cathode Material in Lithium Ion Batteries. *Adv. Energy Mater.* **2014**, *4*, 1300787.

(20) Xu, C.; Märker, K.; Lee, J.; Mahadevegowda, A.; Reeves, P. J.; Day, S. J.; Groh, M. F.; Emge, S. P.; Ducati, C.; Layla Mehdi, B.; Tang, C. C.; Grey, C. P. Bulk Fatigue Induced by Surface Reconstruction in Layered Ni-Rich Cathodes for Li-Ion Batteries. *Nat. Mater.* **2020**, *20*, 84.

(21) Lin, F.; Markus, I. M.; Nordlund, D.; Weng, T.-C.; Asta, M. D.; Xin, H. L.; Doeff, M. M. Surface Reconstruction and Chemical Evolution of Stoichiometric Layered Cathode Materials for Lithium-Ion Batteries. *Nat. Commun.* **2014**, *5*, 3529.

(22) Moryson, Y.; Walther, F.; Sann, J.; Mogwitz, B.; Ahmed, S.; Burkhardt, S.; Chen, L.; Klar, P. J.; Volz, K.; Fearn, S.; Rohnke, M.; Janek, J. Analyzing Nanometer-Thin Cathode Particle Coatings for Lithium-Ion Batteries—The Example of TiO_2 on NCM622. *ACS Appl. Energy Mater.* **2021**, *4*, 7168.

(23) Cho, J.; Kim, T.-J.; Kim, J.; Noh, M.; Park, B. Synthesis, Thermal, and Electrochemical Properties of $AlPO_4$-Coated $LiNi_{0.8}Co_{0.1}Mn_{0.1}O_2$ Cathode Materials for a Li-Ion Cell. *J. Electrochem. Soc.* **2004**, *151*, A1899.

(24) Shi, S. J.; Tu, J. P.; Mai, Y. J.; Zhang, Y. Q.; Tang, Y. Y.; Wang, X. L. Structure and Electrochemical Performance of CaF_2 Coated $LiMn_{1/3}Ni_{1/3}Co_{1/3}O_2$ Cathode Material for Li-Ion Batteries. *Electrochim. Acta* **2012**, *83*, 105−112.

(25) Hall, D. S.; Gauthier, R.; Eldesoky, A.; Murray, V. S.; Dahn, J. R. New Chemical Insights into the Beneficial Role of Al_2O_3 Cathode Coatings in Lithium-Ion Cells. *ACS Appl. Mater. Interfaces* **2019**, *11*, 14095.

(26) David, L.; Dahlberg, K.; Mohanty, D.; Ruther, R. E.; Huq, A.; Chi, M.; An, S. J.; Mao, C.; King, D. M.; Stevenson, L.; Wood, D. L. Unveiling the Role of Al_2O_3 in Preventing Surface Reconstruction During High-Voltage Cycling of Lithium-Ion Batteries. *ACS Appl. Energy Mater.* **2019**, *2*, 1308.

(27) Han, B.; Key, B.; Lipton, A. S.; Vaughey, J. T.; Hughes, B.; Trevey, J.; Dogan, F. Influence of Coating Protocols on Alumina-Coated Cathode Material: Atomic Layer Deposition versus Wet-Chemical Coating. *J. Electrochem. Soc.* **2019**, *166*, A3679−A3684.

(28) Negi, R. S.; Celik, E.; Pan, R.; Stäglich, R.; Senker, J.; Elm, M. T. Insights into the Positive Effect of Post-Annealing on the Electrochemical Performance of Al_2O_3-Coated Ni-Rich NCM Cathodes for Lithium-Ion Batteries. *ACS Appl. Energy Mater.* **2021**, *4*, 3369−3380.

(29) Karayaylali, P.; Tatara, R.; Zhang, Y.; Chan, K.-L.; Yu, Y.; Giordano, L.; Maglia, F.; Jung, R.; Lund, I.; Shao-Horn, Y. Editors' Choice—Coating-Dependent Electrode-Electrolyte Interface for Ni-Rich Positive Electrodes in Li-Ion Batteries. *J. Electrochem. Soc.* **2019**, *166*, A1022−A1030.

(30) Chen, Z.; Qin, Y.; Amine, K.; Sun, Y.-K. Role of Surface Coating on Cathode Materials for Lithium-Ion Batteries. *J. Mater. Chem.* **2010**, *20*, 7606.

(31) Guilmard, M.; Croguennec, L.; Denux, D.; Delmas, C. Thermal Stability of Lithium Nickel Oxide Derivatives. Part I: $Li_xNi_{1.02}O_2$ and $Li_xNi_{0.89}Al_{0.16}$ O_2 (x = 0.50 and 0.30). *Chem. Mater.* **2003**, *15*, 4476−4483.

(32) Croguennec, L.; Bains, J.; Bréger, J.; Tessier, C.; Biensan, Ph.; Levasseur, S.; Delmas, C. Effect of Aluminum Substitution on the Structure, Electrochemical Performance and Thermal Stability of $Li_{1+x}(Ni_{0.40}Mn_{0.40}Co_{0.20-z}Al_z)_{1-x}O_2$. *J. Electrochem. Soc.* **2011**, *158*, A664.

(33) Zhou, F.; Zhao, X.; Lu, Z.; Jiang, J.; Dahn, J. R. The Effect of Al Substitution on the Reactivity of Delithiated $LiNi_{1/3}Mn_{1/3}Co_{(1/3-z)}Al_zO_2$ with Non-Aqueous Electrolyte. *Electrochem. Commun.* **2008**, *10*, 1168−1171.

(34) Wilcox, J. D.; Rodriguez, E. E.; Doeff, M. M. The Impact of Aluminum and Iron Substitution on the Structure and Electrochemistry of $Li(Ni_{0.4}Co_{0.2-y}M_yMn_{0.4})O_2$ Materials. *J. Electrochem. Soc.* **2009**, *156*, A1011.

(35) Han, B.; Key, B.; Lapidus, S. H.; Garcia, J. C.; Iddir, H.; Vaughey, J. T.; Dogan, F. From Coating to Dopant: How the Transition Metal Composition Affects Alumina Coatings on Ni-Rich Cathodes. *ACS Appl. Mater. Interfaces* **2017**, *9*, 41291−41302.

(36) Xiong, D. J.; Hynes, T.; Ellis, L. D.; Dahn, J. R. Effects of Surface Coating on Gas Evolution and Impedance Growth at $Li[Ni_xMn_yCo_{1-x-y}]O_2$ Positive Electrodes in Li-Ion Cells. *J. Electrochem. Soc.* **2017**, *164*, A3174−A3181.

(37) Zhu, W.; Huang, X.; Liu, T.; Xie, Z.; Wang, Y.; Tian, K.; Bu, L.; Wang, H.; Gao, L.; Zhao, J. Ultrathin Al_2O_3 Coating on $LiNi_{0.8}Co_{0.1}Mn_{0.1}O_2$ Cathode Material for Enhanced Cycleability at Extended Voltage Ranges. *Coatings* **2019**, *9*, 92.

(38) Cho, J.; Kim, Y. J.; Park, B. $LiCoO_2$ Cathode Material That Does Not Show a Phase Transition from Hexagonal to Monoclinic Phase. *J. Electrochem. Soc.* **2001**, *148*, A1110−A1115.

(39) Cho, J.; Kim, Y. J.; Park, B. Novel $LiCoO_2$ Cathode Material with Al_2O_3 Coating for a Li Ion Cell. *Chem. Mater.* **2000**, *12*, 3788−3791.

(40) Chen, C.; Yao, W.; He, Q.; Ashuri, M.; Kaduk, J.; Liu, Y.; Shaw, L. Tunable $LiAlO_2$ /Al_2O_3 Coating through a Wet-Chemical Method To Improve Cycle Stability of Nano-$LiCoO_2$. *ACS Appl. Energy Mater.* **2019**, *2*, 3098−3113.

(41) Han, B.; Paulauskas, T.; Key, B.; Peebles, C.; Park, J. S.; Klie, R. F.; Vaughey, J. T.; Dogan, F. Understanding the Role of Temperature and Cathode Composition on Interface and Bulk: Optimizing Aluminum Oxide Coatings for Li-Ion Cathodes. *ACS Appl. Mater. Interfaces* **2017**, *9*, 14769−14778.

(42) Han, B.; Dunlop, A. R.; Trask, S. E.; Key, B.; Vaughey, J. T.; Dogan, F. Tailoring Alumina Based Interphases on Lithium Ion Cathodes. *J. Electrochem. Soc.* **2018**, *165*, A3275−A3283.

(43) Wen, X.; Liang, K.; Tian, L.; Shi, K.; Zheng, J. Al_2O_3 Coating on $Li_{1.256}Ni_{0.198}Co_{0.082}Mn_{0.689}O_{2.25}$ with Spinel-Structure Interface Layer for Superior Performance Lithium Ion Batteries. *Electrochim. Acta* **2018**, *260*, 549−556.

(44) Chen, B.; Ma, X.; Chen, M.; Bullen, D.; Wang, J.; Arsenault, R.; Wang, Y. Systematic Comparison of Al^{3+} Modified $LiNi_{0.6}Mn_{0.2}Co_{0.2}O_2$ Cathode Material from Recycling Process. *ACS Appl. Energy Mater.* **2019**, *2*, 8818−8825.

(45) Jung, R.; Morasch, R.; Karayaylali, P.; Phillips, K.; Maglia, F.; Stinner, C.; Shao-Horn, Y.; Gasteiger, H. A. Effect of Ambient Storage on the Degradation of Ni-Rich Positive Electrode Materials (NMC811) for Li-Ion Batteries. *J. Electrochem. Soc.* **2018**, *165*, A132−A141.

(46) Veith, M. Molecular Precursors for (Nano) Materials—a One Step Strategy. *J. Chem. Soc., Dalton Trans.* **2002**, *12*, 2405−2412.

(47) d'Espinose de Lacaillerie, J.-B.; Fretigny, C.; Massiot, D. MAS NMR Spectra of Quadrupolar Nuclei in Disordered Solids: The Czjzek Model. *J. Magn. Reson.* **2008**, *192*, 244−251.

(48) Massiot, D.; Fayon, F.; Capron, M.; King, I.; Le Calvé, S.; Alonso, B.; Durand, J.-O.; Bujoli, B.; Gan, Z.; Hoatson, G. Modelling One- and Two-Dimensional Solid-State NMR Spectra: Modelling 1D and 2D Solid-State NMR Spectra. *Magn. Reson. Chem.* **2002**, *40*, 70−76.

(49) Coelho, A. A. TOPAS and TOPAS-Academic : An Optimization Program Integrating Computer Algebra and Crystallographic Objects Written in C++. *J. Appl. Crystallogr.* **2018**, *51*, 210−218.

(50) *Handbook of Practical X-Ray Fluorescence Analysis*; Beckhoff, B., Ed.; Springer: Berlin; New York, 2006.

(51) Boyes, E. D. Analytical Potential of EDS at Low Voltages. *Microchim. Acta* **2002**, *138*, 225−234.

(52) Baer, D. R.; Artyushkova, K.; Cohen, H.; Easton, C. D.; Engelhard, M.; Gengenbach, T. R.; Greczynski, G.; Mack, P.; Morgan, D. J.; Roberts, A. XPS Guide: Charge Neutralization and Binding Energy Referencing for Insulating Samples. *J. Vac. Sci. Technol., A* **2020**, *38*, 031204.

(53) Verdier, S.; El Ouatani, L. E.; Dedryvère, R.; Bonhomme, F.; Biensan, P.; Gonbeau, D. XPS Study on Al_2O_3- and $AlPO_4$-Coated $LiCoO_2$ Cathode Material for High-Capacity Li Ion Batteries. *J. Electrochem. Soc.* **2007**, *154*, A1088−A1099.

(54) Appapillai, A. T.; Mansour, A. N.; Cho, J.; Shao-Horn, Y. Microstructure of $LiCoO_2$ with and without "$AlPO_4$ " Nanoparticle Coating: Combined STEM and XPS Studies. *Chem. Mater.* **2007**, *19*, 5748−5757.

(55) Lebens-Higgins, Z.; Faenza, N.; Mukherjee, P.; Sallis, S.; Badway, F.; Pereira, N.; Schlueter, C.; Lee, T.-L.; Cosandey, F.; Amatucci, G.; Piper, L. F. J. Electrochemical and Thermal Stress of $LiNi_{0.8}Co_{0.15}Al_{0.05}O_2$ Electrodes: Evolution of Aluminum Surface Environments. *ECS Trans.* **2017**, *80*, 197−206.

(56) Leifer, N.; Srur-Lavi, O.; Matlahov, I.; Markovsky, B.; Aurbach, D.; Goobes, G. $LiNi_{0.8}Co_{0.15}Al_{0.05}O_2$ Cathode Material: New Insights via ^{7}Li and ^{27}Al Magic-Angle Spinning NMR Spectroscopy. *Chem. Mater.* **2016**, *28*, 7594−7604.

(57) Lee, S. K.; Park, S. Y.; Yi, Y. S.; Moon, J. Structure and Disorder in Amorphous Alumina Thin Films: Insights from High-Resolution Solid-State NMR. *J. Phys. Chem. C* **2010**, *114*, 13890−13894.

(58) Dogan, F.; Vaughey, J. T.; Iddir, H.; Key, B. Direct Observation of Lattice Aluminum Environments in Li Ion Cathodes $LiNi_{1-y-z}Co_yAl_zO_2$ and Al-Doped $LiNi_xMn_yCo_zO_2$ via ^{27} Al MAS NMR Spectroscopy. *ACS Appl. Mater. Interfaces* **2016**, *8*, 16708−16717.

(59) Sarou-Kanian, V.; Gleizes, A. N.; Florian, P.; Samélor, D.; Massiot, D.; Vahlas, C. Temperature-Dependent 4-, 5- and 6-Fold Coordination of Aluminum in MOCVD-Grown Amorphous Alumina Films: A Very High Field ^{27}Al-NMR Study. *J. Phys. Chem. C* **2013**, *117*, 21965−21971.

(60) Müller, D.; Gessner, W.; Scheler, G. Chemical Shift and Quadrupole Coupling of the ^{27}Al NMR Spectra of $LiAIO_2$ Polymorphs. *Polyhedron* **1983**, *2*, 1195−1198.

(61) Wohlmuth, D.; Epp, V.; Bottke, P.; Hanzu, I.; Bitschnau, B.; Letofsky-Papst, I.; Kriechbaum, M.; Amenitsch, H.; Hofer, F.; Wilkening, M. Order vs. Disorder—a Huge Increase in Ionic Conductivity of Nanocrystalline $LiAlO_2$ Embedded in an Amorphous-like Matrix of Lithium Aluminate. *J. Mater. Chem. A* **2014**, *2*, 20295−20306.

(62) Zheng, J.; Ye, Y.; Liu, T.; Xiao, Y.; Wang, C.; Wang, F.; Pan, F. Ni/Li Disordering in Layered Transition Metal Oxide: Electrochemical Impact, Origin, and Control. *Acc. Chem. Res.* **2019**, *52*, 2201−2209.

(63) Sicklinger, J.; Metzger, M.; Beyer, H.; Pritzl, D.; Gasteiger, H. A. Ambient Storage Derived Surface Contamination of NCM811 and NCM111: Performance Implications and Mitigation Strategies. *J. Electrochem. Soc.* **2019**, *166*, A2322−A2335.

(64) Märker, K.; Reeves, P. J.; Xu, C.; Griffith, K. J.; Grey, C. P. Evolution of Structure and Lithium Dynamics in $LiNi_{0.8}Mn_{0.1}Co_{0.1}O_2$ (NMC811) Cathodes during Electrochemical Cycling. *Chem. Mater.* **2019**, *31*, 2545−2554.

(65) Li, H.; Liu, A.; Zhang, N.; Wang, Y.; Yin, S.; Wu, H.; Dahn, J. R. An Unavoidable Challenge for Ni-Rich Positive Electrode Materials for Lithium-Ion Batteries. *Chem. Mater.* **2019**, *31*, 7574−7583.

(66) Trease, N. M.; Seymour, I. D.; Radin, M. D.; Liu, H.; Liu, H.; Hy, S.; Chernova, N.; Parikh, P.; Devaraj, A.; Wiaderek, K. M.; Chupas, P. J.; Chapman, K. W.; Whittingham, M. S.; Meng, Y. S.; Van der Van, A.; Grey, C. P. Identifying the Distribution of Al^{3+} in $LiNi_{0.8}Co_{0.15}Al_{0.05}O_2$. *Chem. Mater.* **2016**, *28*, 8170−8180.

(67) Lee, S. K.; Lee, S. B.; Park, S. Y.; Yi, Y. S.; Ahn, C. W. Structure of Amorphous Aluminum Oxide. *Phys. Rev. Lett.* **2009**, *103*, 095501.